

Automated Simulation of Electrode Processes: Quantitative Mechanistic Analysis via Working Surface Interpolation

John A. Alden and Richard G. Compton*

Physical and Theoretical Chemistry Laboratory, Oxford University, South Parks Road, Oxford OX1 3QZ, U.K.

Received: March 20, 1997[®]

An efficient *automated* simulation of the transport-limited electrolysis in a channel flow cell, based on the multigrid method, is developed and is used to compute the working curve for the transport-limited current within the L  v  que approximation. An accurate universal two-dimensional working surface (making neither the L  v  que approximation nor ignoring axial diffusion) is presented for the steady-state transport-limited current from which the simulated response may be interpolated. The multigrid simulation is extended to include homogenous ECE kinetics and a working surface is presented for analysis of this mechanism within the L  v  que approximation. This is then modified using a Gauss–Newton method to solve the nonlinear EC₂E system for which an analogous working surface is generated. The effect of axial diffusion on the measurement of rate constants for these mechanisms is discussed. The merits of bilinear, cubic convolution, bicubic spline, and artificial neural network methods are assessed as interpolation methods for working surfaces. Working surface interpolation is shown to be a viable cost-effective alternative to repeated simulation methods, especially for problems of more than one dimension. A free data-processing service using the working surface data together with a suitable interpolation method is available via the World Wide Web (<http://physchem.ox.ac.uk:8000/wwwda>).

1. Introduction

The repeated simulation of physical problems in more than one dimension can be immensely resource-intensive in terms of CPU time and memory.^{1,2} Therefore, a two- or three-dimensional analogue of the commercial 1-D electrochemical simulation packages currently available (such as DigiSim) is probably not feasible with the current or even next generation level of personal computer technology. Here we present an alternative approach. The partial differential equations describing many physical problems may be reduced to a dimensionless form so that the experimental observable may be represented in terms of its dimensionless parameters as a working curve³, surface,^{4,5} or hypersurface. Once this surface has been generated using a powerful workstation or supercomputer, the simulated response may be reconstructed from the stored surface using an appropriate interpolation algorithm. Utilizing the Internet, the surfaces need not even be stored on a personal computer—the data can be stored on a World Wide Web (WWW) server which can perform the interpolation and return the results.

The convective-diffusion occurring at a channel microband electrode presents a challenging two-dimensional problem that, due to inherent asymmetry, is not amenable to conformal mappings such as those used to simulate diffusion-only mass transport to a microdisc^{6,7} or microband electrode.^{8,9} This means that even with an exponentially expanding grid mesh in the *y* coordinate, a large number of finite difference nodes are required for an accurate simulation, especially when simulating multi-species problems where each species may have a different spatial distribution. The introduction of direct steady-state simulations, such as the strongly implicit procedure (SIP)¹⁰ followed by the more efficient and stable multigrid method,¹¹ has considerably reduced the amount of CPU time required but repeated simulations (for example, to fit a rate constant to experimental data sets) are still prohibitively expensive both in terms of memory and CPU time.

Simulations based on the multigrid method are developed for electron transfer reactions occurring at a microband electrode in a channel flow cell with following first- or second-order homogenous kinetics. The simulation of a transport-limited electron-transfer reaction using the multigrid method is optimized using an expanding *y* grid and routines for automatic geometric convergence. This allows the range of an electron transfer working curve (which was derived and calculated in a previous paper¹²) within the L  v  que approximation¹³ to be extended to the full range of channel flow experiments by utilizing the more accurate and efficient multigrid simulation.

The two-dimensional working surface resulting from removal of the L  v  que approximation is also generated across the full range of channel flow experiments and is used as the basis to assess the ranges across which approximate analytical methods are valid. Comprehensive summaries of the results of the E, ECE, and EC₂E simulations are presented here in the form of working surfaces which may be used directly (in digital form via the World Wide Web) by experimentalists without the need for further simulation. These allow effective simulation of a mechanism instantaneously without requiring any knowledge of numerical modelling or expensive computer hardware. The full data sets are available for download on the World Wide Web (<http://physchem.ox.ac.uk:8000/research/comp/wsurl.html>) together with forms to submit data to programs which perform kinetic analysis using the working surfaces.

Interpolation methods are assessed for use with working surfaces. These range from the easily programmed bilinear interpolation method through the more sophisticated methods of cubic convolution and bicubic splines, to the use of artificial neural networks^{14,15} which are readily available commercially.

2. Theory

Steady-state simulations based on the multigrid method are developed for the three following mechanisms occurring at a microband electrode in a channel flow cell: (a) A transport-limited electron transfer reaction, a linear one-species problem;

[®] Abstract published in *Advance ACS Abstracts*, November 1, 1997.

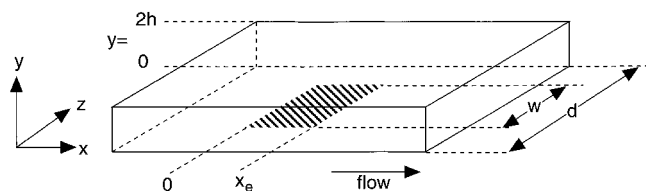


Figure 1. Schematic of the channel flow cell showing dimensions and the coordinate system employed.

(b) a transport-limited ECE reaction, a linear three-species problem which may be solved sequentially; (c) A transport-limited EC₂E reaction, a nonlinear three-species problem which may be solved sequentially. For each of these reactions the current can be expressed in terms of one or two dimensionless parameters allowing the mechanism to be characterised by a working curve or surface.

2.1. Dimensionless Variables, Parameterisation of Current. For a transport-limited electrolysis (for example a one-electron reduction)



at a channel electrode with z large enough that diffusion the z coordinate can be ignored (Figure 1), the convective-diffusion equation is

$$\frac{\partial a}{\partial t} = D \frac{\partial^2 a}{\partial x^2} + \frac{\partial^2 a}{\partial y^2} - v_x \frac{\partial a}{\partial x} = 0 \quad (2)$$

where $a = [A]/[A]_{\text{bulk}}$, D is the diffusion coefficient, and v_x is the solution velocity in the x -direction. The coordinates x , y , and z are defined in Figure 1. Under laminar flow conditions, when a Poiseuille flow profile has fully developed, v_x is given by

$$v_x = \frac{3}{4} \frac{V_f}{dh} \left[1 - \frac{(y-h)^2}{h^2} \right] \quad (3)$$

where V_f is the volume flow rate, $2h$ is the height of the cell (in the y coordinate), and d is the width of the cell (in the z coordinate).

As shown in ref 12, eq 2 may be reduced into a dimensionless form:

$$\frac{\partial^2 a}{\partial \chi^2} + \frac{\partial^2 a}{\partial \psi^2} - \frac{3}{4} p_2 (p_1)^2 \psi [2 - p_1 \psi] \frac{\partial a}{\partial \chi} = 0 \quad (4)$$

where

$$\chi = \frac{x}{x_e}, \quad \psi = \frac{y}{x_e}, \quad p_1 = \frac{x_e}{h}, \quad \text{and} \quad p_2 = \frac{V_f}{dD} \quad (5)$$

and x_e is the width of the microband electrode (in the x coordinate). The dimensionless current (Nusselt number) is given by

$$N = \frac{I}{F[A]_{\text{bulk}} D w} \quad (6)$$

where I is the current, w is the length of the microband electrode in the z coordinate (see Figure 1), and F is the Faraday constant. Since the current is given by

$$I = n F w D [A]_{\text{bulk}} \int_0^1 \frac{\partial a}{\partial \psi} \bigg|_{\psi=0} d\chi \quad (7)$$

and ψ is set to zero and χ disappears once the integral is

evaluated, the Nusselt number is purely a function of p_1 and p_2 , hence this relationship can be represented as a two-dimensional working surface. If the L  v  que approximation is made,

$$y_x = \frac{3}{4} \frac{V_f}{dh} 2 \left[1 - \frac{y-h}{h} \right] = y \frac{3}{2} \frac{V_f}{dh^2} \quad (8)$$

the dimensionless mass transport equation reduces to

$$\frac{\partial^2 a}{\partial \chi^2} + \frac{\partial^2 a}{\partial \psi^2} - \frac{3}{2} p_2 (p_1)^2 \psi \frac{\partial a}{\partial \chi} = 0 \quad (9)$$

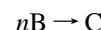
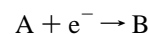
and thus N simplifies to a unique function of the shear Peclet number P_s :

$$P_s = \frac{3}{2} p_1^2 p_2 = \frac{3 x_e^2 V_f}{2 h^2 d D} \quad (10)$$

Therefore the current response can be represented as a working curve. In the absence of axial diffusion the function may be solved for giving the classical Levich equation:¹⁶

$$N_{\text{LEVICH}} = 0.925 \left(\frac{2}{3} \right)^{1/3} P_s^{1/3} \quad (11)$$

For an ECE or EC₂E reaction (written as a reduction),



(where $n = 1$ defines an ECE reaction and $n = 2$ defines an EC₂E reaction), the steady-state combined mass transport and kinetic equations are

$$\frac{\partial a}{\partial t} = D \frac{\partial^2 a}{\partial x^2} + D \frac{\partial^2 a}{\partial y^2} - v_x \frac{\partial a}{\partial x} = 0 \quad (13)$$

$$\frac{\partial b}{\partial t} = D \frac{\partial^2 b}{\partial x^2} + D \frac{\partial^2 b}{\partial y^2} - v_x \frac{\partial b}{\partial x} - n k_c b^n = 0 \quad (14)$$

$$\frac{\partial c}{\partial t} = D \frac{\partial^2 c}{\partial x^2} + D \frac{\partial^2 c}{\partial y^2} - v_x \frac{\partial c}{\partial x} + k_c b^n = 0 \quad (15)$$

where $b = [B]/[A]_{\text{bulk}}$, $c = [C]/[A]_{\text{bulk}}$, and k_c is given by

$$k_c = k[A]_{\text{bulk}}^{n-1} \quad (16)$$

The ratio N_{eff} of the total current (arising from the transport-limited electrolysis of species A and C) to that of a simple electron transfer reaction can be shown¹² to depend on the same parameters as those of the electron transfer reaction and also on the dimensionless rate constant:

$$K_{\text{ECE}} = P_s^{-2/3} \frac{k x_e^2}{D} \quad \text{or} \quad K_{\text{EC}_2\text{E}} = P_s^{-2/3} \frac{k x_e^2}{D} [A]_{\text{bulk}} \quad (17)$$

Under the L  v  que approximation, N_{eff} is consequently a function of P_s and either K_{ECE} or $K_{\text{EC}_2\text{E}}$. These relationships may be conveniently summarized in terms of a two-dimensional working surface.

2.2. Simulation Details. The five-point steady-state finite difference equation was solved using the multigrid method,

TABLE 1: Boundary Conditions^a

description	nodes	boundary condition	finite difference implementation
upstream: bulk concentration	all $j, k = 0$	$[A]_{x \leftarrow -\infty} = [A]_{\text{bulk}}$	$a_{j,0} = 0$
downstream: no flux	all $j, k = \text{NK}$	$\frac{\partial a}{\partial x} _{x \leftarrow \infty} = 0$	$a_{j,\text{NK}} = a_{j,\text{NK}-1}$
wall opposite electrode: no flux	$j = \text{NJ}$, all k	$\frac{\partial a}{\partial y} _{y=2h} = 0$	$a_{\text{NJ},k} = a_{\text{NJ}-1,k}$
upstream of electrode: no flux	$j = 0, k \leq \text{AL}(\text{KE})$	$\frac{\partial a}{\partial y} _{y=0} = 0$	$a_{0,k} = a_{1,k}$
electrode surface: transport limited electrolysis	$j = 0, \text{AL}(\text{KE}) + 1 \leq k \leq (\text{AL} + 1)\text{KE}$	$[A]_{y=0} = 0$	$a_{0,k} = 0$
downstream of electrode: no flux	$j = 0, k > (\text{AL} + 1)\text{KE}$	$\frac{\partial a}{\partial y} _{y=0} = 0$	$a_{0,k} = a_{1,k}$

^a AL and BE are the number of electrode lengths upstream and downstream of the electrode, respectively. $a_{j,k}$ denotes a node on the finite grid (j is the index in the y coordinate and k is the index in the x coordinate). The finite difference grid stops one node short of the boundaries¹¹ (running from $k = 1$ to NGX , $j = 1$ to NGY) thus the boundary nodes which are not simulated (NJ and NK) are given by $\text{NJ} = \text{NGY} + 1$ and $\text{NK} = \text{NGX} + 1$. The number of nodes across the electrode KE is given by $\text{NGX}/(\text{AL} + \text{BE} + 1)$.

MGD1 (NAG library routine D03EDF¹⁷) as described in an earlier publication.¹¹ In order to maximize the number of coarse-grid levels in the multigrid scheme, the number of nodes were expressed (in NAG notation) as

$$\begin{aligned} \text{NGX} &= \text{XP}2^{\text{LV}} + 1 \text{ in the } x \text{ direction, and} \\ \text{NGY} &= \text{YP}2^{\text{LV}} + 1 \text{ in the } y \text{ direction} \end{aligned} \quad (18)$$

where the integer variables NGX and NGY represent the number of nodes simulated in the x and y coordinates, respectively. The integer variable LV (number of coarse-grid levels) is made as high as possible for a given number of nodes, reducing the integer variables XP and YP accordingly. The boundary conditions used are shown in Table 1.

An exponentially expanding y -grid using the coordinate transformation:

$$\psi = \frac{\left(\frac{y}{2\phi h} + 1\right)^\gamma - 2^\gamma}{1 - 2^\gamma} \quad (19)$$

was used to improve computational efficiency and accuracy (exactly as implemented in earlier publications¹⁸), where γ is an expansion factor and ϕ is the fraction of the channel simulated. An expanding x -grid based on an inverse hyperbolic tangent function (as used by Pastore et al.¹⁹) was tried to improve convergence efficiency at low P_s , but was found to cause divergence of the multigrid algorithm. Therefore a simple Cartesian x -grid was used.

The convection term was discretised by an upwind scheme to ensure diagonal dominance of the coefficient matrix (defined as $[A]$ in ref 11) and thus stability¹⁷ of the multigrid method at high Peclet numbers, where $\lambda_v > \lambda_x$. Thus the finite difference representation of eq 2 is given by

$$\begin{aligned} -[\lambda_x + \lambda_v]a_{j,k-1} - [\lambda_{yd} + \lambda_{ys}]a_{j-1,k} + \\ [2\lambda_x + 2\lambda_{yd} + \lambda_v]a_{j,k} - [\lambda_{yd} - \lambda_{ys}]a_{j+1,k} - \lambda_x a_{j,k+1} = 0 \end{aligned} \quad (20)$$

where

$$\begin{aligned} \lambda_x &= \frac{D}{(\Delta x)^2} \\ \lambda_{yd} &= \frac{D}{(\Delta \psi)^2} \left[\frac{1}{2\phi h} \gamma \left(\frac{y}{2\phi h} + 1 \right)^{\gamma-1} \right]^2 \end{aligned}$$

$$\begin{aligned} \lambda_{ys} &= \frac{D}{\Delta \psi} \frac{\left(\frac{1}{2\phi h}\right)^2 \gamma(\gamma-1) \left(\frac{y}{2\phi h} + 1\right)^{\gamma-2}}{1 - 2^\gamma} \\ \lambda_v &= \frac{v_x}{\Delta x} \end{aligned} \quad (21)$$

and $\Delta x = x_0/\text{NGX}(\text{AL} + \text{BE} + 1)$, $\Delta \psi = 2\phi h/\text{NGY}$. The numerical dispersion error due to upwinding was found to be negligible ($<0.01\%$), compared with a centrally differenced convection term.

Subroutines were written to automatically find the optimal channel fraction (ϕ) and upstream/downstream space (AL electrode lengths) by initially simulating a very large ($\phi = 1$, $\text{AL} = 450$) value then scanning the resulting concentration profile to detect where the normalised concentration deviated significantly from unity (a threshold of 0.999 was used) and thus the extent of the simulation space required. A second iteration was conducted starting from twice the optimal value calculated in the first iteration in order to obtain a good estimate when the optimal parameters were small. Previously these values were found by "trial and error", making the generation of several hundred points for a working surface prohibitively laborious.

Simulations were written in C compiled with maximum optimization and linked to the NAG FORTRAN library before being executed on a DEC Alpha, Silicon Graphics Indigo², and Indy. A typical memory requirement was 131MB for a simulation with $\text{LV} = 9$; $\text{XP} = 4$; $\text{YP} = 1$, for which the simulation of each species took approximately 10 mins of CPU time on a DEC Alpha.

2.3. Homogeneous Kinetics. For an ECE or EC₂E process where the electrolysis of species A and C transport-limited, the mass-transport equation for each species may be solved sequentially: species A is independent thus can be solved first. The electrode surface boundary condition of species B depends on the surface concentration of species A (known when B is solved) and the irreversible step forming species C from species B can be applied to B and C separately (B is known when C is solved).

The boundary conditions used for these simulations are the same as the for the simulation of the transport-limited current for all species except those shown in Table 2. The implicit finite difference forms of eqs 13–15 (with upwind convection) are

TABLE 2: Boundary Conditions Specific to the ECE and EC₂E Simulations

description	nodes	definition	finite difference definition
upstream: zero B concentration	all $j, k = 0$	$[B]_{x \rightarrow -\infty} = 0$	$b_{j,0} = 0$
upstream: zero C concentration	all $j, k = 0$	$[C]_{x \rightarrow -\infty} = 0$	$c_{j,0} = 0$
electrode surface: flux of B	$j = 0, \text{AL}(\text{KE} + 1) \leq k \leq (\text{AL} + 1)\text{KE}$	$\left. \frac{\partial[A]}{\partial y} \right _{y=0} = - \left. \frac{\partial[B]}{\partial y} \right _{y=0}$	$b_{0,k} = a_{1,k} + b_{1,k}$
away = flux of A in			

$$-[\lambda_x + \lambda_v]a_{j,k-1} - [\lambda_{yd} + \lambda_{ys}]a_{j-1,k} + [2\lambda_x + 2\lambda_{yd} + \lambda_v]a_{j,k} - [\lambda_{yd} - \lambda_{ys}]a_{j+1,k} - \lambda_x a_{j,k+1} = 0 \quad (22)$$

$$-[\lambda_x + \lambda_v]b_{j,k-1} - [\lambda_{yd} + \lambda_{ys}]b_{j-1,k} + [2\lambda_x + 2\lambda_{yd} + \lambda_v]b_{j,k} - [\lambda_{yd} - \lambda_{ys}]b_{j+1,k} - \lambda_x b_{j,k+1} - nk_c(b_{j,k})^n = 0 \quad (23)$$

$$-[\lambda_x + \lambda_v]c_{j,k-1} - [\lambda_{yd} + \lambda_{ys}]c_{j-1,k} + [2\lambda_x + 2\lambda_{yd} + \lambda_v]c_{j,k} - [\lambda_{yd} - \lambda_{ys}]c_{j+1,k} - \lambda_x c_{j,k+1} + k_c(b_{j,k})^n = 0 \quad (24)$$

For the ECE process, the finite difference equations may be solved as they stand using the multigrid method, but the finite difference equation for species B in the EC₂E case is nonlinear. A system of nonlinear equations may be solved iteratively using the Gauss–Newton method.²⁰ Starting from an initial approximation for the concentration of b , $b^{(0)}$, successive approximations may be obtained from the formula

$$\mathbf{J}(\mathbf{b}^{(i)})\mathbf{b}^{(i+1)} = \mathbf{J}(\mathbf{b}^{(i)})\mathbf{b}^{(i)} - T(\mathbf{b}^{(i)}) = \mathbf{R} \quad (25)$$

where (i) is the iteration number,

$$\mathbf{b} = \begin{pmatrix} b_{1,1} \\ b_{2,1} \\ \vdots \\ b_{\text{NGY},\text{NGX}} \end{pmatrix}$$

$$\mathbf{T}(\mathbf{b}) = \begin{bmatrix} t_{1,1}(\mathbf{b}) \\ t_{2,1}(\mathbf{b}) \\ \vdots \\ t_{\text{G},\text{NGX}}(\mathbf{b}) \end{bmatrix}$$

and $t_{j,k}(\mathbf{b})$ denotes a general finite difference equation. The Jacobian is given by

$$\mathbf{J}(\mathbf{b}) = \begin{pmatrix} \frac{\partial t_{1,1}}{\partial b_{1,1}} & \frac{\partial t_{1,1}}{\partial b_{2,1}} & \cdots & \frac{\partial t_{1,1}}{\partial b_{\text{NGY},\text{NGX}}} \\ \frac{\partial t_{2,1}}{\partial b_{1,1}} & \frac{\partial t_{2,1}}{\partial b_{2,1}} & \cdots & \frac{\partial t_{2,1}}{\partial b_{\text{NGY},\text{NGX}}} \\ \vdots & \vdots & \ddots & \vdots \\ \frac{\partial t_{\text{NGY},\text{NGX}}}{\partial b_{1,1}} & \frac{\partial t_{\text{NGY},\text{NGX}}}{\partial b_{2,1}} & \cdots & \frac{\partial t_{\text{NGY},\text{NGX}}}{\partial b_{\text{NGY},\text{NGX}}} \end{pmatrix}$$

From eq 23:

$$t_{j,k}(\mathbf{b}) = \mathbf{A}_{j,k}^1 b_{j,k-1} + \mathbf{A}_{j,k}^3 b_{j-1,k} + \mathbf{A}_{j,k}^4 b_{j,k} - 2k_c(b_{j,k})^2 + \mathbf{A}_{j,k}^5 b_{j+1,k} + \mathbf{A}_{j,k}^7 b_{j,k+1} \quad (26)$$

where $\mathbf{A}_{j,k}^{1-7}$ are the seven multigrid stencil coefficients^{11,17} at each finite difference node. The five nonzero terms in the Jacobian are

$$\frac{\partial t_{j,k}}{\partial b_{j,k-1}} = \mathbf{A}_{j,k}^1, \quad \frac{\partial t_{j,k}}{\partial b_{j-1,k}} = \mathbf{A}_{j,k}^3, \quad \frac{\partial t_{j,k}}{\partial b_{j,k}} = \mathbf{A}_{j,k}^4 - 2k_c b_{j,k},$$

$$\frac{\partial t_{j,k}}{\partial b_{j+1,k}} = \mathbf{A}_{j,k}^5, \quad \frac{\partial t_{j,k}}{\partial b_{j,k+1}} = \mathbf{A}_{j,k}^7 \quad (27)$$

Substituting eqs 26 and 27 into eq 25 we obtain

$$\mathbf{R}_{j,k} = \mathbf{A}_{j,k}^1 b_{j,k-1}^{(i)} + \mathbf{A}_{j,k}^3 b_{j-1,k}^{(i)} + \mathbf{A}_{j,k}^4 b_{j,k}^{(i)} - 2k_c(b_{j,k}^{(i)})^2 + \mathbf{A}_{j,k}^5 b_{j+1,k}^{(i)} + \mathbf{A}_{j,k}^7 b_{j,k+1}^{(i)} - (\mathbf{A}_{j,k}^1 b_{j,k-1}^{(i)} + \mathbf{A}_{j,k}^3 b_{j-1,k}^{(i)} + \mathbf{A}_{j,k}^4 b_{j,k}^{(i)} - 2k_c(b_{j,k}^{(i)})^2 + \mathbf{A}_{j,k}^5 b_{j+1,k}^{(i)} + \mathbf{A}_{j,k}^7 b_{j,k+1}^{(i)}) \quad (28)$$

Thus

$$\mathbf{J}_{j,k}(b_{j,k}^{(i)})b_{j,k}^{(i+1)} = 2k_c b_{j,k}^{(i)} \quad (29)$$

This is in a form that can be solved by the multigrid method with the elements (see the NAG library for a definition of \mathbf{A} , \mathbf{f} , and \mathbf{u}):

$$\mathbf{A}_{j,k}^1 = -(\lambda_x + \lambda_v)$$

$$\mathbf{A}_{j,k}^2 = 0$$

$$\mathbf{A}_{j,k}^3 = -(\lambda_{yd} + \lambda_{ys})$$

$$\mathbf{A}_{j,k}^4 = 2\lambda_x + 2\lambda_{yd} + \lambda_v - 4k_c(b_{j,k}^{(i)})^2$$

$$\mathbf{A}_{j,k}^5 = -(\lambda_{yd} + \lambda_{ys})$$

$$\mathbf{A}_{j,k}^6 = 0$$

$$\mathbf{A}_{j,k}^7 = -\lambda_s$$

$$\mathbf{f}_{j,k} = 2k_c b_{j,k}^{(i)}$$

$$\mathbf{u}_{j,k} = b_{j,k}^{(i+1)}$$

The importance of the expanding y-grid should be stressed for the simulation of fast homogenous kinetics. At high rate constants, the reaction layer (the region near the electrode surface where there is a significant concentration of species B) is very thin in comparison to the diffusion layer (the region where species A is depleted by electrolysis). With a Cartesian y-grid this means that the number of nodes in the y coordinate must be increased dramatically to ensure convergence at high rate constants. The expanding y-grid allows most of the simulation nodes to be placed in the reaction layer while still spanning the diffusion layer.

Moreover, if extremely high rate constants are sought (this was not necessary for the simulations presented in this paper), it is possible to use different expansion parameters for species A and both species B and C, since species B is only related to A by the flux at the electrode surface. This allows species B and C to have a more rapidly expanding grid function mimicking the steep concentration gradient that occurs near the electrode surface at high rate constants. However, unlike species B, the concentration distribution of species C is not confined to the reaction layer, so the expanding grid for species B and C would have to compromise between their two distribution functions.

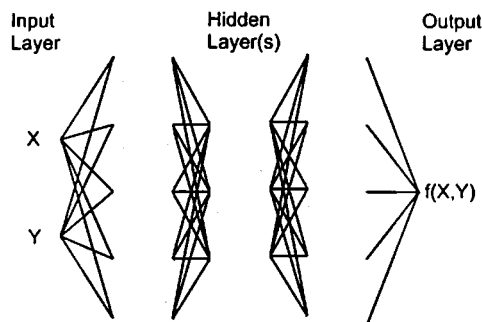


Figure 2. A two-input, one output fully connected artificial neural network used for reconstruction of a surface of $f(x,y)$ from a set of x and y points. The number of hidden layers and nodes in the hidden layers are adjustable variables.

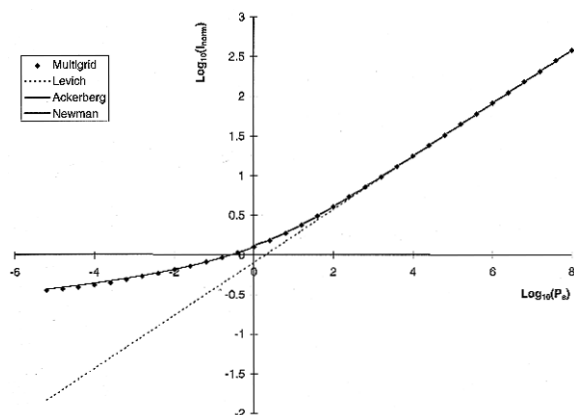


Figure 3. Electron transfer working curve, applicable under conditions where the Lévêque approximation is valid. $\text{Log}_{10} P_s$ ranges from -4 to 8 spanning from a flow rate of $5.76 \times 10^{-4} \text{ cm}^3 \text{ s}^{-1}$ over an electrode of length $0.25 \mu\text{m}$ to a flow rate of $2.25 \text{ cm}^3 \text{ s}^{-1}$ over an electrode of length 4 mm , for a typical channel of height 0.06 cm and width 0.6 cm with a typical nonaqueous diffusion coefficient of $1 \times 10^{-5} \text{ cm}^2 \text{ s}^{-1}$. The approximate equations of Levich, Newman and, Ackerberg are shown for comparison.

TABLE 3: Parameters Used in the Simulation of the Electron-Transfer Reaction

electrode length	x_e	$5 \mu\text{m}$
electrode width	w	0.4 cm
channel height	$2h$	calculated from p_1
channel width	d	0.6 cm
diffusion coefficient	D	$1 \times 10^{-5} \text{ cm}^2 \text{ s}^{-1}$
bulk concentration	$[A]_{\text{bulk}}$	$1 \times 10^{-6} \text{ mol cm}^{-3}$
flow rate	V_f	calculated from p_2
number of nodes in x coordinate	NGX	2049
number of nodes in y coordinate	NGY	513
grid expansion parameter	γ'	10

2.4. Interpolation Methods. Interpolation was conducted on the decadic logarithm of the current so that the fractional error from interpolation would be an approximately uniform across the surface. (If interpolation had been conducted on the current value itself, the percentage error would have been larger for smaller current values). For ECE and EC₂E mechanisms, the interpolation was conducted on the N_{eff} value rather than on its logarithm, since N_{eff} spans a narrow range of magnitude.

Four methods were investigated. The first, bilinear interpolation using the INTERPOLATE routine in IDL V4 (Floating point systems; Berks, U.K.), was chosen because it is the simplest and most easily programmed two-dimensional interpolation method. Interpolation using bicubic convolution was also assessed (using the /CUBIC option of the IDL INTERPOLATE routine).

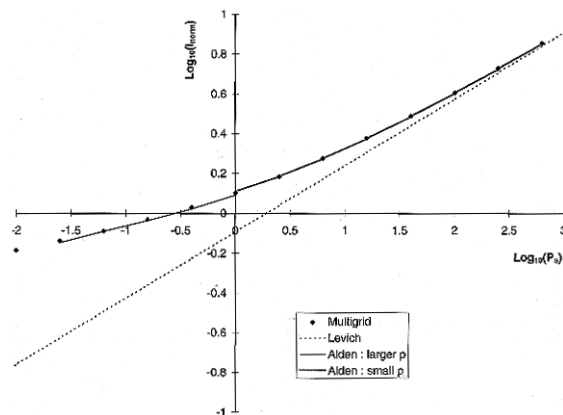


Figure 4. Comparison of the expressions and simulations in ref 12 with the multigrid simulations.

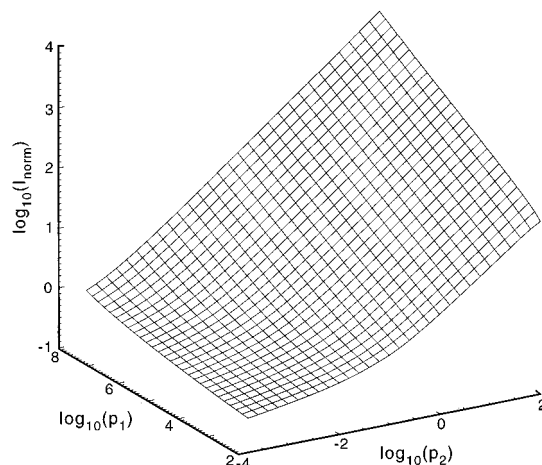


Figure 5. Electron-transfer working surface plotted as the \log_{10} of the Nusselt number as a function of $\log_{10} p_1$ and $\log_{10} p_2$. $\log_{10} p_1$ ranges from -2.4 to 2.0 corresponding to electrode lengths of $1.2 \mu\text{m}$ – 30 mm in a typical channel of height $(2h)$ 0.06 cm . $\log_{10} p_2$ ranges from 2.0 to 6.0 corresponding to flow rates of 6×10^{-4} – $6 \text{ cm}^3 \text{ s}^{-1}$ in a typical cell of width d 0.6 cm with a typical diffusion coefficient in a nonaqueous solvent of $1 \times 10^{-5} \text{ cm}^2 \text{ s}^{-1}$.

Bicubic spline interpolation was conducted using the NAG library routines E02DAF to fit the spline surface and E02DBF to evaluate it at the sought coordinates. These routines were used with the parameters suggested in the NAG FORTRAN library manual²¹ to produce “interpolating splines”. These give more accurate reconstruction of values near the ends of the range than a natural bicubic spline interpolation such as the routine E01ACF²¹ (where the second derivatives are zero at the ends of the ranges).

The last method investigated was an artificial neural network (ANN). A simple back-propagating neural network with 2 inputs, 1 output, and a number of internal nodes (shown in Figure 2) serves as a nonlinear regression method in which the variable coefficients (connection weightings) are optimized for the data set via the training procedure. For a fully connected network (which was used in all cases) with 2 inputs and 1 output, the number of connections are given by

$$3l_1 \quad \text{for one hidden layer}$$

$$2l_1 + l_1l_2 + l_2 \quad \text{for two hidden layers}$$

$$2l_1 + l_2(l_1 + l_3) + l_3 \quad \text{for three hidden layers}$$

where l_1 , l_2 , and l_3 are the numbers of nodes in the first, second, and third hidden layers, respectively.

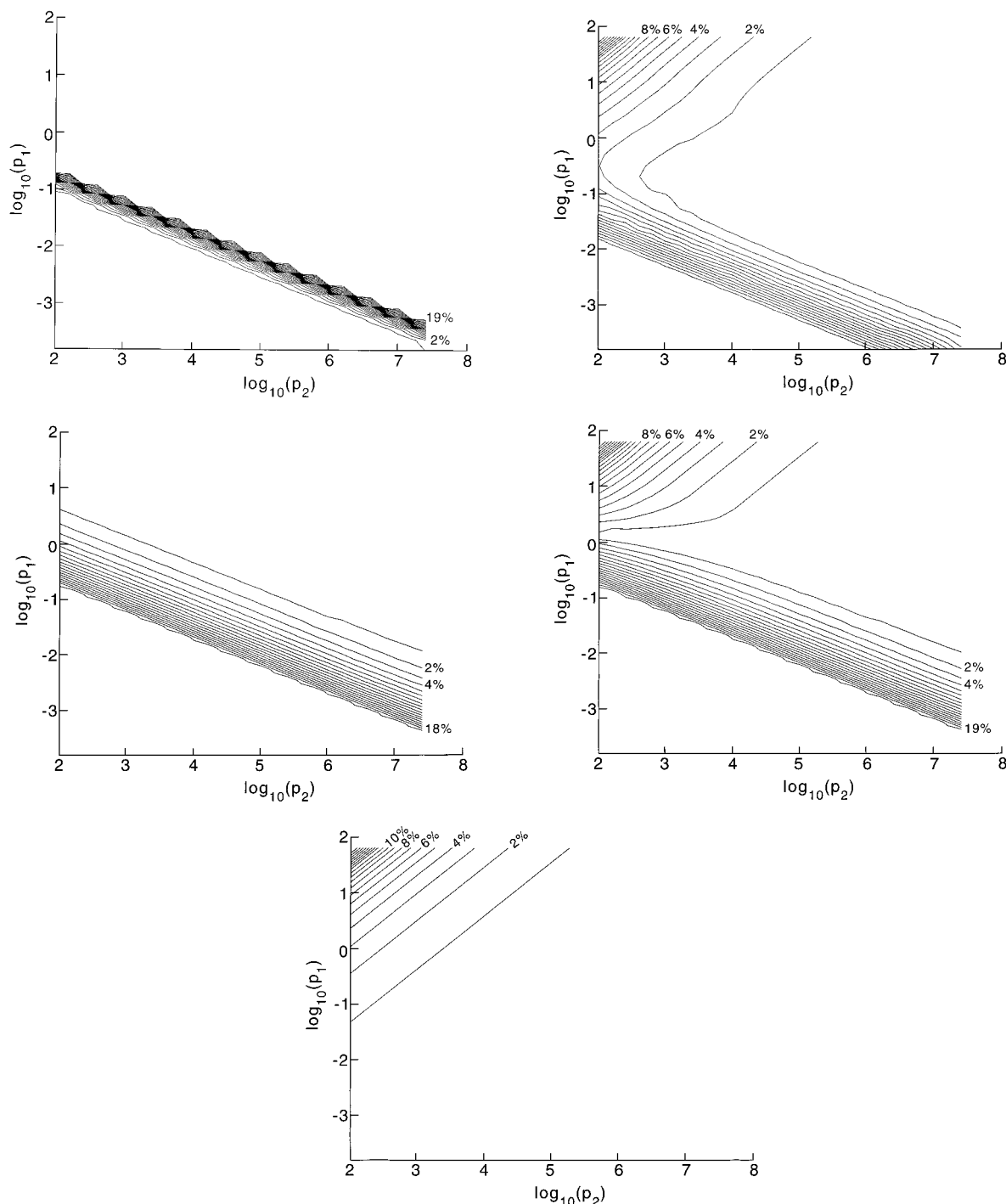


Figure 6. Difference from the surface in Figure 5 (expressed as percentage error) for (a) the Ackerberg equation, (b) the Newman equation, (c) BI simulations, and (d) the Levich equation. The percentage error of the Levich surface relative to the BI surface is also shown e.

The commercial package ARD Propagator V1.0 (ARD corporation; Columbia, MD) was used for ANN interpolation. In all cases a validation data set (the points which were to be interpolated) was used when training the neural network in order to prevent over training. In order to be used with the neural network, the data was normalized to values suitable for the network transfer functions. Sigmoidal transfer functions were used, taking values between zero and 1, so the data was normalized between 0.05 and 0.95 before use with the ANN.

3. Results and Discussion

In this section we present the results of the simulations as working curves and surfaces and compare the data to any previously published analytical expressions and numerical

simulations (see also Table 3). This not only confirms the accuracy of our simulations, but also allows the ranges across which the other approximate methods are valid to be ascertained.

3.1. Transport-Limited Electron Transfer. An asymptotic expression for the Nusselt number has been derived by Ackerman²² et al. for mass transport at low-shear Peclet numbers, valid²³ for $P_s < 1$.

$$N_{\text{ACKERBERG}} = \pi g(P_s)(1 - 0.04633P_s g(P_s))$$

where $g(P_s) = 1/(\ln[4/\sqrt{P_s}] + 1.0559)$ (30)

Newman²⁴ has derived an expression for high-shear Peclet numbers, valid²³ for $P_s > 1$.

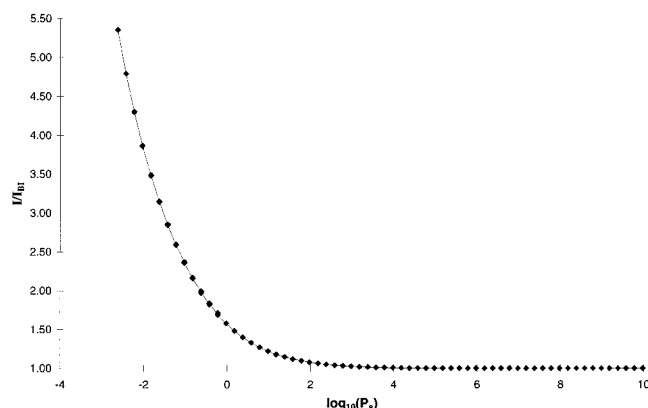


Figure 7. A plot of the ratio of the multigrid and BI simulations, showing the effects of axial diffusion can be expressed as a unique function of the shear Peclet number P_s .

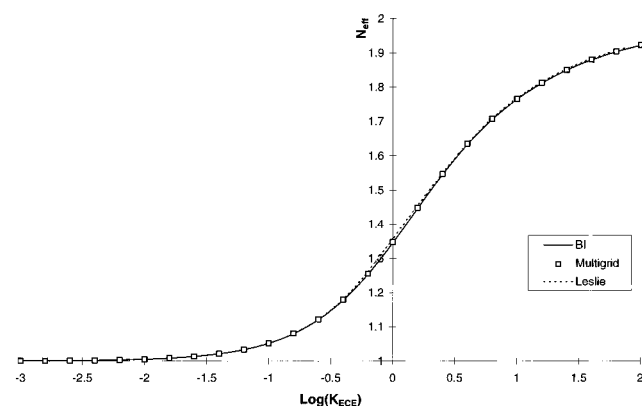


Figure 8. ECE working curve at high shear Peclet number ($P_s = 4.4$) calculated from multigrid, BI, and Leslie's approximate expressions.

$$N_{\text{NEWMAN}} = 0.8075P_s^{1/3} + 0.7058P_s^{-1/6} - 0.1984P_s^{-1/3} \quad (31)$$

3.1.1. Transport-Limited Current within the L  v  que Approximation. Figure 3 shows the working curve for the transport-limited current plotted as the decadic logarithm of the Nusselt number as a function of $\log_{10}(P_s)$. Various analytical expressions are shown for comparison: the Levich, Ackerberg, and Newman equations agree well with simulations in their respective domains. This has also been confirmed using experimental data from Compton et al.²⁵ by Zhang et al.²³ In prior work,¹² the expression by Newman was shown to agree with SIP simulations at high P_s (low p) while an expression derived by Aoki²⁶ did not agree even if corrected for a downstream contribution. The low- and high- p regressions of the SIP data based on the form of the Newman equation from ref 12 are plotted in Figure 4 together with the SIP and multigrid data. The agreement is excellent verifying those expressions and the convergence of the early SIP simulations with the more easily converged multigrid method utilizing an expanding y -grid.

3.1.2. Transport-Limited Current without Approximations. Figure 5 shows the working surface for the electron-transfer reaction. In the region of very low P_s (<0.1) the Ackerberg equation was used in preference to simulation data, as it was not possible to converge simulations to within 1% due to the excessive amount of memory that would be necessary to accommodate the several thousand (or tens of thousands of) nodes required to converge the simulation in the x coordinate. The region where the Levich equation is valid can be seen as an oblique planar area at high p_1 and p_2 . Note that at *extremely*

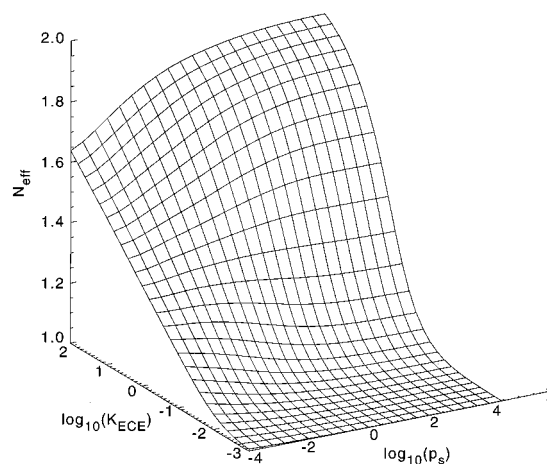


Figure 9. ECE working surface plotted as the limiting current divided by that of a transport-limited electrolysis (N_{eff}) as a function of the \log_{10} of the shear Peclet number (P_s) and the \log_{10} of the dimensionless rate constant (K_{ECE}). $\log_{10}(P_s)$ ranges from -4 to 4.4 corresponding to a flow rate of $5.76 \times 10^{-4} \text{ cm}^3 \text{ s}^{-1}$ over an electrode of length $0.25 \text{ }\mu\text{m}$, and a flow rate of $3.6 \times 10^{-2} \text{ cm}^3 \text{ s}^{-1}$ over an electrode of length 0.5 mm , respectively for a typical cell with the same parameters as in Figure 3. $\log_{10}(K_{\text{ECE}})$ ranges from -3 to 2 which corresponds to k ranging from 3.4×10^{-2} to $3.4 \times 10^3 \text{ s}^{-1}$ at $P_s = -4$ and k ranging from 3.4×10^{-3} to $3.4 \times 10^2 \text{ s}^{-1}$ at $P_s = 4.4$.

TABLE 4: Parameters Used in the Simulation of ECE and EC₂E Mechanisms^a

number of nodes in x coordinate	NGX	2049
number of nodes in y coordinate	NGY	513
grid expansion parameter	γ	10
rate constant	k	calculated from K_{ECE} or $K_{\text{EC}_2\text{E}}$

^a All other parameters were the same as for the simulation of a transport-limited electrolysis in Table 3.

high p_1 (not shown since this corresponds to a thin-layer cell rather than channel flow-cell) the Levich equation breaks down and $I \propto V_f$.

Figure 6a–d are contour plots of the percentage error using (a) Ackerberg's eq 30; (b) Newman's eq 31; (c) simulations using the backward implicit method,^{27,28} which neglects axial diffusion but does not make the L  v  que approximation, and d the Levich equation. Also shown is e, the difference between the Levich and BI surfaces (again expressed as a percentage error, relative to BI), which can be interpreted as the effect of making the L  v  que approximation. As anticipated, Ackerberg's expression is valid in the region of low P_s and Newman's is valid at high P_s . Notice also that Newman's expression breaks down when the L  v  que approximation no longer holds, at low rates of convection.

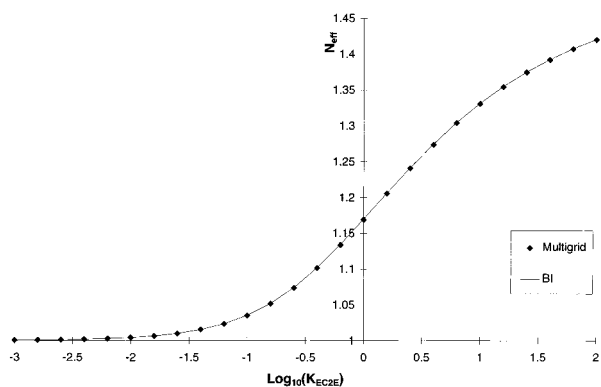
Comparing Figure 6c–e, it can be seen that the effects of axial diffusion and breakdown of the L  v  que approximation do not overlap significantly. This is even more apparent if one plots all the data from c against the shear Peclet number as is shown in Figure 7. All the data lies on a single curve implying that for the channel flow-cell experiments in this range, *axial diffusion effects only need to be calculated within the L  v  que approximation* as we have done in section 3.11 and ref 12.

For this reason, studies of homogenous kinetics were limited to conditions where the L  v  que approximation may be used. BI simulations can be used to simulate homogenous kinetics²⁸ at low rates of mass transport where the L  v  que approximation breaks down and axial diffusion effects are negligible.

3.2. ECE within the L  v  que Approximation. Leslie et al.²⁹ derived three approximate expressions (accurate to within

TABLE 5: Training and Validation Data Sets for Interpolation

surface	x coordinate	x_{\min}	x_{\max}	Δx	y coordinate	y_{\min}	y_{\max}	Δy
ET training	$\log_{10} p_1$	-2.4	2	0.2	$\log_{10} p_2$	2	6	0.2
ET validation	$\log_{10} p_1$	-2.3	1.9	0.2	$\log_{10} p_2$	2.1	5.9	0.2
ECE training	$\log_{10} P_s$	-4	4.4	0.4	$\log_{10} K_{\text{ECE}}$	-3	2	0.2
ECE validation	$\log_{10} P_s$	-3.8	4.2	0.4	$\log_{10} K_{\text{ECE}}$	-2.9	1.9	0.2
EC ₂ E training	$\log_{10} P_s$	-4	4.4	0.4	$\log_{10} K_{\text{EC}_2\text{E}}$	-3	2	0.2
EC ₂ E validation	$\log_{10} P_s$	-3.8	4.2	0.4	$\log_{10} K_{\text{EC}_2\text{E}}$	-2.9	1.9	0.2

**Figure 10.** EC₂E working curve calculated from multigrid and BI simulations at high shear Péclet number ($P_s = 4.4$).

to 0.4%) for the working curve of N_{eff} in terms of K_{ECE} which are applicable when axial diffusion can be neglected:

$$N_{\text{eff}} = 2 - 0.736K_{\text{ECE}}^{-1/2} + 0.0613K_{\text{ECE}}^{-2} \quad \text{for } K_{\text{ECE}} \geq 3.96$$

$$N_{\text{eff}} = 1.358 + 0.4831 \log K_{\text{ECE}} \quad \text{for } 0.59 < K_{\text{ECE}} < 3.96$$

$$N_{\text{eff}} = 1 + 1.0552K_{\text{ECE}} - 0.309K_{\text{ECE}}^2 + 0.150K_{\text{ECE}}^3 \quad \text{for } K_{\text{ECE}} \leq 0.59 \quad (32)$$

These are compared with simulations using the multigrid and backward implicit methods in Figure 8 for a \log_{10} shear Péclet number of 4.4. The two simulation lines overlay exactly, indicating that the effect of axial diffusion is negligible at this shear Péclet number. The analytical expressions can be seen to work well in their respective ranges. Figure 9 shows the ECE working surface generated from the multigrid simulations. As one would expect, the effect of increasing axial diffusion (decreasing P_s) is to stretch the working curve so that kinetic discrimination is improved. See Table 4 for parameters.

3.3. EC₂E within the Lévêque Approximation. Multigrid and backward implicit simulations are compared in Figure 10, again agreement is excellent. Note that the backward implicit simulations, if implemented using explicit kinetics (based on concentrations at node $j, k-1$) as in ref 28, require an ever larger number of nodes in the x coordinate as the rate constant increases. For the ECE reaction the kinetics can be easily made implicit (based on concentrations at node j, k) utilizing the transformation

$$\mathbf{b}_{j,k} = \mathbf{b}_{j,k} - k_c \quad (33)$$

instead of

$$\mathbf{d}_{j,k} = \mathbf{d}_{j,k} + k_c \quad (34)$$

(where $\mathbf{b}_{j,k}$ is the coefficient of $\mathbf{b}_{i,k}$ and $\mathbf{d}_{j,k}$ is the coefficient of $\mathbf{b}_{i,k-1}$ —for a more detailed definition see ref 28). For the EC₂E reaction, the Gauss–Newton method can be implemented with the BI method, as is described above for the multigrid method, to allow kinetics to be simulated implicitly.

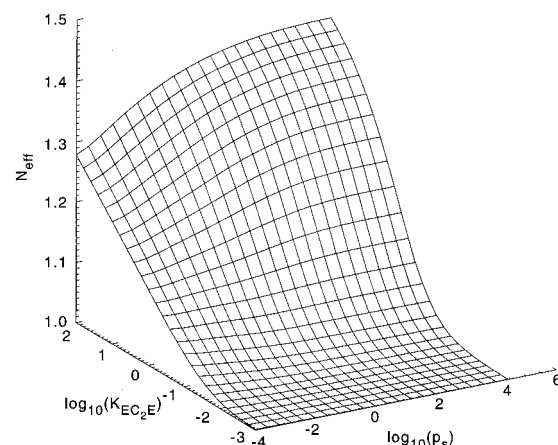
**Figure 11.** EC₂E working surface plotted as the limiting current divided by that of a transport-limited electrolysis (N_{eff}) as a function of the \log_{10} of the shear Péclet number (P_s) and the \log_{10} of the dimensionless second order rate constant ($K_{\text{EC}_2\text{E}}$). $\log_{10}(K_{\text{EC}_2\text{E}})$ ranges from -3 to 2, which corresponds to k ranging from 3.4×10^{-2} to $3.4 \times 10^3 \text{ cm}^3 \text{ mol}^{-1} \text{ s}^{-1}$ at $P_s = -4$ and k ranging from 3.4×10^{-3} to $3.4 \times 10^2 \text{ cm}^3 \text{ mol}^{-1} \text{ s}^{-1}$ at $P_s = 4.4$.

Figure 11 shows the EC₂E working surface generated from the multigrid simulations. The trend is very similar to that observed for the ECE case.

3.4. Interpolation of Working Surface Data. In order to evaluate the performance of various interpolation methods, a pair of surface data sets was simulated for each mechanism, the second (validation) surface being offset half an interval in both the x and y directions from the first (training) data set, as shown in Table 5. The observable at the coordinates corresponding to the validation data set could then be interpolated using the training data set and the error measured. The parameters used in ARD Propagator for neural network fitting are shown in Table 6. Suitable learning rate and momentum factors were deduced empirically.

The interpolation errors for various network architectures are shown in Table 7. The first column corresponds to the number of nodes in each layer—two in the input layer and one in the output layer in all cases, but a variation in the number of hidden layers and nodes in the hidden layers. As one would expect, fitting improves and training time increases with the overall number of hidden-layer nodes as the number of variable parameters (weights) increases. As one would perhaps expect,

TABLE 6: Parameters for ARD Propagator Neural Network

parameter	value
transfer functions	sigmoidal
random seed	0
connectivity	full
learning rule	generalized delta
learning rate	0.4
momentum factor	0.5
training patterns order	random
training cycles	100 000
initial weights	-1 to 1
input noise	none

TABLE 7: Interpolation Errors on Each of the Three Surfaces for Various ANN Architectures

surface		transport-limited electron transfer		ECE		EC ₂ E	
NN architecture	no. of connections	mean	max	mean	max	mean	max
2 10 1	30	0.554%	3.485%	0.119%	0.405%	0.036%	0.187%
2 5 5 1	40	0.371%	2.464%	0.067%	0.297%	0.023%	0.162%
2 3 4 3 1	33	0.433%	4.171%	0.082%	0.404%	0.034%	0.192%
2 20 1	60	0.549%	3.457%	0.099%	0.464%	0.034%	0.197%
2 10 10 1	130	0.371%	2.200%	0.049%	0.273%	0.022%	0.161%
2 6 7 7 1	111	0.370%	2.414%	0.048%	0.311%	0.019%	0.172%
2 40 1	120	0.664%	3.811%	0.105%	0.419%	0.044%	0.158%
2 20 20 1	460	0.316%	2.18%	0.0382%	0.265%	0.021%	0.150%
2 13 14 13 1	403	0.327%	2.03%	0.0429%	0.236%	0.021%	0.142%

TABLE 8: Interpolation Errors on Each of the Three Surfaces for Various Interpolation Methods

interpolation method	transport-limited electron transfer		ECE		EC ₂ E	
	mean	max	mean	max	mean	max
linear	0.134%	0.927%	0.060%	0.228%	0.027%	0.134%
cubic convolution	0.525%	5.925%	0.066%	0.465%	0.030%	0.279%
bicubic spline	0.043%	0.894%	0.012%	0.225%	0.007%	0.134%
neural network ^a	0.316%	2.18%	0.0382%	0.265%	0.021%	0.142%

^a Using optimal architecture from Table 7.

the mean error decreases as the number of connections (and hence “fitting” parameters) increases. The optimal architecture appears to be with two hidden layers as this gives rise to the maximum number of connections for a given number of nodes, though three hidden layers give a lower maximum error with a large number of nodes.

Table 8 shows the percentage error in current for interpolation on each of the three surfaces using the three methods. The success of simple bilinear interpolation on the electron transfer surface can be rationalised by the planarity of the surface in the region where the Levich equation holds.

Bicubic spline interpolation is clearly the superior method, though linear and ANN interpolation both give highly respectable results. For the ECE and EC₂E surface the “maximum” error occurs at very low P_s (<-3.8) where there is a minor turning point in the data due to slightly imperfect convergence (maximum error of 3–4% in this region compared with $<1\%$ elsewhere). This is due to the extremely high number of nodes required to converge the Cartesian grid the x direction under these conditions where there is a massive amount of axial diffusion relative to the size of the electrode. With “perfect” (infinitely converged) data the results from bicubic spline and linear interpolation would be considerably better, however rather than rejecting data from this region we chose evaluate the interpolation methods on data with a realistic imperfection.

4. Conclusions

An accurate and efficient multigrid method has been developed for two-dimensional steady-state finite difference simulations of a channel microband electrode. These simulations have allowed a high-resolution (28×30 point) working surface to be generated across the full range of experimental parameters for the transport-limited electrolysis in a channel flow cell, which permits quantitative assessment of approximate analytical methods. The extension to processes involving coupled homogenous kinetics is assisted by application of the Gauss–Newton method which allows systems with second-order homogenous kinetics to be simulated in a fully implicit manner. Working surfaces have also been generated for ECE and EC₂E reactions, allowing the quantitative analysis of channel microband electrode experiments on these systems. The working surfaces, together with an appropriate interpolation algorithm, allow experimental responses to be predicted accurately and

instantaneously by the nonspecialist. Of the interpolation methods investigated, bicubic spline interpolation was shown to be superior to both bilinear interpolation and artificial neural networks. Cubic convolution interpolation performed relatively poorly in all cases. Bilinear interpolation was found to give highly satisfactory results for minimal programming effort and CPU time and is therefore the choice method for data sets of this resolution. For lower resolution surfaces, bicubic spline interpolation would probably be the optimal method. For problems where the experimental observable must be represented by a higher dimension (hyper) surface the choice is more restricted—only linear interpolation and ANNs can be readily extended to higher dimensions. An interpolation and kinetic analysis service is provided via the World Wide Web: <http://physchem.ox.ac.uk:8000/wwwda>

Acknowledgment. We thank Keble College for a scholarship for J.A.A. EPSRC support via Grant GR/L34167 is gratefully acknowledged.

References and Notes

- (1) Britz, D. *J. Electroanal. Chem.* **1996**, 406, 15.
- (2) Rudolph, M. In *Physical Electrochemistry*; Rubenstein, I., Ed.; Marcel Dekker: New York, 1995; p 81.
- (3) Unwin, P. R.; Compton, R. G. *J. Electroanal. Chem.* **1988**, 145, 287.
- (4) Alden, J. A.; Compton, R. G.; Dryfe, R. A. W. *J. Electroanal. Chem.* **1995**, 397, 11.
- (5) Bidwell, M. J.; Alden, J. A.; Compton, R. G. *J. Electroanal. Chem.* **1996**, 414, 247.
- (6) Micheal, A. C.; Wightman, R. M.; Amatore, C. A. *J. Electroanal. Chem.* **1989**, 26, 33.
- (7) Amatore, C. R.; Fosset, B. *J. Electroanal. Chem.* **1992**, 328, 21.
- (8) Deakin, M. R.; Wightman, R. M.; Amatore, C. A. *J. Electroanal. Chem.* **1986**, 215, 49.
- (9) Fosset, B.; Amatore, C. A.; Bartlet, J.; Wightman, R. M. *Anal. Chem.* **1991**, 63, 1403.
- (10) Compton, R. G.; Dryfe, R. A. W.; Wellington, R. G.; Hirst, J. J. *Electroanal. Chem.* **1995**, 383, 13.
- (11) Alden, J. A.; Compton, R. G. *J. Electroanal. Chem.* **1996**, 415, 1.
- (12) Alden, J. A.; Compton, R. G. *J. Electroanal. Chem.* **1996**, 404, 27.
- (13) L  v  que, M. A. *Ann. Mines, Mem.* **1928**, 12/13, 201.
- (14) Cartwright, H. M. *Applications of Artificial Intelligence in Chemistry*; Oxford University Press: Oxford, 1993.
- (15) Duch, W.; Dierckson, G. H. F. *Comput. Phys. Commun.* **1994**, 82, 91.
- (16) Levich, V. G. *Physicochemical Hydrodynamics*; Prentice-Hall: Englewood Cliffs, NJ, 1962; p 112.

(17) NAG Fortran Library Mark 15; National Algorithms Group: Oxford; Vol. 3, Section D03EDF, p 1. The Numerical Algorithms Group have an information desk which may be contacted by e-mail: infodesk@nag.co.uk.

(18) Bidwell, M. J.; Alden, J. A.; Compton, R. G. *J. Electroanal. Chem.* **1996**, 414, 247.

(19) Pastore, L.; Magno, F.; Amatore, C. A. *J. Electroanal. Chem.* **1991**, 301, 1.

(20) Rudolph, M. *J. Electroanal. Chem.* **1992**, 338, 85.

(21) NAG Fortran Library Mark 15, E01 Introduction, Section 3.3.1. See: (ref 1).

(22) Ackerman, R. C.; Patel, R. D.; Gupta, S. K. *J. Fluid. Mech.* **1978**, 86, 49.

(23) Zhang, W.; Stone, H. A.; Sherwood, J. D. *J. Phys. Chem.* **1996**, 100, 9462.

(24) Newman J. *J. Electroanal. Chem.* **1973**, 6, 279.

(25) Compton, R. G.; Fisher, A. C.; Wellington, R. G.; Dobson, P. J.; Leigh, P. A. *J. Phys. Chem.* **1995**, 99, 10942.

(26) Aoki, K.; Tokuda, K.; Matsuda, H. *J. Electroanal. Chem.* **1987**, 217, 33.

(27) Anderson, J. L.; Moldoveanu, S. *J. Electroanal. Chem.* **1984**, 179, 107.

(28) Compton, R. G.; Pilkington, M. B. G.; Stearn, G. M. *J. Chem. Soc., Faraday Trans.* **1988**, 84, 2155.

(29) Leslie, W. M.; Alden, J. A.; Compton, R. G.; Silk, T. *J. Phys. Chem.* **1996**, 100, 14130.